# Theoretical and Experimental Characterization of Structures of MnAu Nanoclusters in the Size Range of 1–3 nm

**Rulong Zhou,[†,‡] Xiaohui Wei,[§] Kai He,[⊥] Jeffrey E. Shield,[∥] David J. Sellmyer,[§] and Xiao Cheng Zeng[†,§,*]**

[†]Department of Chemistry and Nebraska Center for Materials and Nanoscience, University of Nebraska, Lincoln, Nebraska 68588, United States, [‡]School of Science and Engineering of Materials, Hefei University of Technology, Hefei, Anhui 230009, China, [§]Department of Physics and Nebraska Center for Materials and Nanoscience, University of Nebraska, Lincoln, Nebraska 68588, United States, [⊥]Department of Materials Science and Engineering, University of Maryland, College Park, Maryland 20742, United States, and [∥]Department of Mechanical and Materials Engineering and Nebraska Center for Materials and Nanoscience, University of Nebraska, Lincoln, Nebraska 68588, United States

**ABSTRACT** Relative stabilities of MnAu magic-number nanoclusters with 55, 147, 309, and 561 atoms and highly symmetric morphologies (cuboctahedron, icosahedron, onion-like, and core–shell, respectively) are investigated based on density functional theory methods. Through an extensive search, spin arrangements on Mn atoms that give rise to lowest-energy clusters are predicted. The antiferromagnetic spin configurations are found to be the most favorable for all morphologies investigated. The energy rankings among MnAu nanoclusters with the same size and Mn/Au ratio but different morphologies are also determined. The $L1_0$ structure is found to be increasingly favorable as the size increases from 1.0 to 2.9 nm, consistent with experimental measurements of MnAu nanoparticles in the size range of 1.8–4.6 nm. The decahedron $L1_0$ morphology is found to be energetically more preferred when the Mn/Au ratio is close to 1:2, whereas the cuboctahedron $L1_0$ morphology is more preferred when the Mn/Au ratio is close to 1:1. The calculated lattice constants are in excellent agreement with high-resolution TEM measurements for MnAu nanoparticles of similar size. Magnetic states of MnAu nanoclusters are predicted to be stable at room temperature based on estimated Curie or Neél temperature.

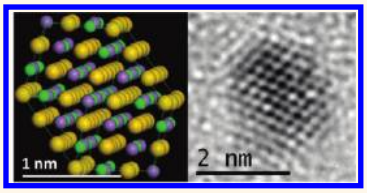


**KEYWORDS:** MnAu nanoclusters · magic-number clusters · $L1_0$ morphology · antiferromagnetic · high-resolution TEM measurements · density functional theory

Manganese is an important transition-metal element due in part to its high magnetic moment. Mn-containing materials can be potentially useful for magnetic applications if the magnetic ordering is sustained. However, it is well-known that bulk manganese is antiferromagnetic (AFM) and thus possesses zero net magnetic moment. Small-sized Mn clusters can exhibit much larger magnetic moments than the bulk due to the large surface-to-volume ratios. Indeed, magnetism of small-sized Mn clusters has been extensively investigated over the past decades.[1−5] Thus far, experimental measurements have shown that free Mn clusters in the size range of 5–99 atoms possess small net magnetic moments.[4,5] Theoretical calculations indicate that, starting from $Mn_5$, the AFM ordering arises, which can lead to reduced total magnetic moments.[2,3] Nevertheless, one possible strategy to sustain large magnetic moments of Mn clusters is to add dopants. For example, it has been recently shown that Ti and V dopants can efficiently increase the net magnetic moments of the $Mn_{13}$ cluster.[6] Previous work suggests that, by coating an atomic-layer gold shell to the $Mn_{13}$ cluster (core), the net magnetic moments of the core–shell clusters can be significantly enhanced due to elongation of the Mn–Mn distances by the gold shell.[7] Another general strategy to enhance magnetic moments of transition-metal nanoparticles is to use noble-metal alloying as reported previously.[8] However, few studies have been reported on the effect of nanoalloying on structural and magnetic properties of Mn nanoclusters beyond 1 nm.

It is known that electronic structures and magnetic properties of nanoclusters are highly dependent on their morphologies. For nanoalloys, both crystalline structures and noncrystalline structures conceivably may exist. The crystalline structures are typically nanosized fragments of bulk crystals. Octahedra or truncated octahedra are common crystalline structures for nanoalloys

* Address correspondence to xzeng1@unl.edu.

Received for review September 30, 2011 and accepted November 22, 2011.

**Published online November 22, 2011**
**10.1021/nn203739d**

that are composed of both transition-metal and noble-metal elements. As for noncrystalline structures, the most common forms are highly symmetric icosahedra, decahedra, and polyicosahedra. For each type of morphology, nanoalloys can also adopt numerous atomic arrangements for each element. The core–shell, multishell, onion-like, and $L1_0$ morphologies, among others, are common elemental arrangements for binary nanoalloys. Moreover, the energetic properties of the MnAu nanoclusters can be influenced not only by their size and shape but also by the Mn/Au ratio. Hence, nanoclusters with multiple morphologies may coexist within particular size ranges (typically within a few nanometers). In light of the importance of understanding structure–function relationship of nanoclusters, it is desirable to investigate size-, morphology-, and composition-dependent evolution of structural and magnetic ordering in the MnAu nanoclusters.

In the past decade, much theoretical effort has been devoted to finding global-minimum structures of small-sized (<1 nm) bimetallic clusters using various global optimization methods.[9−15] For larger-sized bimetallic nanoclusters beyond 1 nm, however, unbiased global search is impractical due to the complexity of the potential energy surface of the nanoclusters. Most theoretical work on large-sized bimetallic clusters focuses on the possible existence of structural transition based on classic molecular dynamics or Monte Carlo simulations.[16−21] Recently, Bochicchio and Ferrando predicted a size-dependent transition to high-symmetry chiral structures in AuCo, AgNi, and AuNi noble/magnetic nanoalloys based on a global optimization search with a semiempirical potential, followed by DFT optimization.[22] Gruner *et al.* investigated size dependence of energetic rankings and magnetic properties of various FePt and CoPt nanoclusters with different morphologies using DFT calculations.[23] Rossi *et al.* predicted a transition to decahedral $L1_0$ structure for the CoPt nanoclusters and an $L1_0$ order to $L1_0$ disorder transition for larger-sized CoPt nanoclusters based on global optimization and canonical Monte Carlo simulations, respectively.[24]

In this work, we have performed a systematic study of size- and morphology-dependent energetic properties and magnetic ordering in MnAu nanoclusters, based on density functional theory (DFT) calculations. We find that antiferromagnetic ordering of spins on Mn atoms is energetically most favorable for all morphologies considered in this work. The $L1_0$ atomic arrangement is predicted to be the most stable for MnAu nanoclusters, starting from the size of 147 atoms (~1.7 nm). Complementary experimental measurements, using high-resolution transmission electron microscopy (HR-TEM), of MnAu nanoparticles in the size range of 1.8–4.6 nm confirm the theoretical prediction.

## MODELS

In this study, our focus is mainly placed on the magic-number clusters $N = 55, 147, 309, 561$, which are known to be highly stable for transition-metal clusters. For each size, six highly symmetric morphologies, namely, icosahedron core–shell (IH-CS), icosahedron onion-like (IH-ON), cuboctahedron core–shell (CH-CS), cuboctahedron $L1_0$ (CH-$L1_0$), decahedron core–shell (DH-CS), and decahedron $L1_0$ (DH-$L1_0$), are examined, similar to Gruner's work.[23] To evaluate relative stabilities among six morphologies, various spin arrangements on Mn atoms are examined, as well. As pointed out above, Mn favors AFM spin ordering for Mn clusters larger than $Mn_5$. However, it is a formidable task to search the ground magnetic state for MnAu cluster containing many Mn atoms since the number of spin configurations increase proportion to $2^{N-1}$, where $N$ is the number of Mn atoms. For small magnetic clusters, it has been shown previously that it is possible to determine the ground spin state of a magnetic cluster by computing its energy as a function of all possible net magnetic moment.[6,7] In this way, there can be a number of spin arrangements for a given magnetic moment. However, for large clusters without high symmetry, this method can still be impractical because for many midranged magnetic moments there exist too many spin configurations and in many of them it is difficult to achieve convergence under the DFT optimization. Nevertheless, for large cluster with high symmetry, the number of distinct spin configurations can be dramatically reduced. As such, it is possible to track spin arrangements of energetically low-lying clusters by examining various symmetric spin configurations.

First, we have performed an extensive search for the low-energy spin states of the MnAu clusters with 147 atoms to determine the lowest-energy spin arrangement. Two approaches were employed to search the low-lying spin states. In the first approach, we initially optimize the structure unrestrictedly with a fixed total magnetic moment whose value ranges from 0 to the highest value possible, with an increment of 10 $\mu_B$. Next, with the obtained spin arrangement on Mn atoms from previous step, the atomic structure is then reoptimized while allowing the magnitude of local magnetic moment to change unrestrictedly but their directions are fixed. As a result, low-lying spin arrangements on Mn atoms with a new value of total magnetic moment can be obtained for a given morphology.

With the goal of attaining low-lying spin arrangements on Mn atoms, we devise an independent second approach by recognizing that neighboring Mn atoms tend to align in opposite directions due to strong AFM interaction between them, and that Mn atoms far apart have little influence on each other. Specifically, we reset the spin direction on each Mn atom manually, to meet the likelihood that spins on neighboring

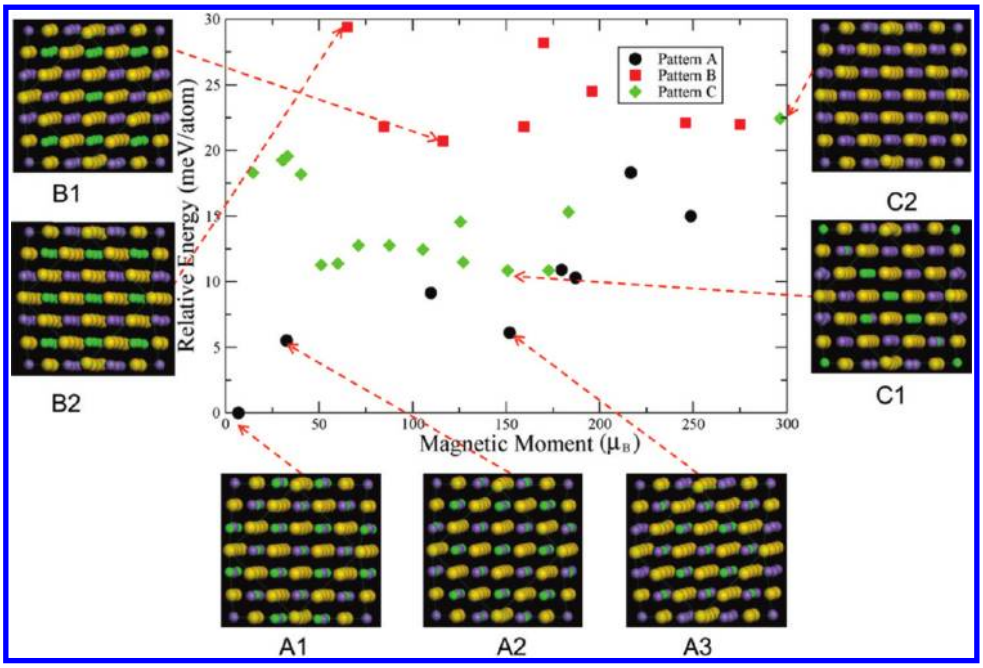


**Figure 1. Calculated relative energies of the $Mn_{67}Au_{80}$ clusters with the CH-$L1_0$ morphology at various spin configurations. Representative configurations (A1−A3, B1, B2, and C1 and C2) for patterns A−C are plotted. Yellow spheres represent gold atoms, and purple and green spheres represent Mn atoms in spin-up and spin-down state, respectively.**

Mn atoms are opposite to each other. Although there can be many different spin configurations generated in the second approach, it turns out that much deeper low-lying states can be located this way.

Having obtained low-lying spin arrangements for all six highly symmetric morphologies of 147 atom MnAu clusters, we optimize structures of larger MnAu clusters of the same morphology. For the magic-number clusters with the same symmetry, we expect their low-lying spin arrangements to retain the same symmetry. Therefore, the same spin arrangements are adopted for larger clusters whose symmetry is the same as that of the 147 atom MnAu clusters.

## RESULTS AND DISCUSSION

**Spin Arrangements in $Mn_{67}Au_{80}$ (1.7 nm) Clusters.** Using the $Mn_{67}Au_{80}$ clusters with the CH-$L1_0$ morphology as a prototype model, relative energies of the 147 atom clusters with different net magnetic moments and spin arrangements are shown in Figure 1. Two distinct patterns of spin arrangements for Mn atoms, named as pattern A and pattern B, are examined. Both patterns entail highly ordered spin arrangements. Configuration A1 and B2 shown in Figure 1 are representative spin arrangements for pattern A and B, where, in A1, every Mn atom entails an opposite spin direction with respect to its nearest-neighbor Mn atoms and, in B2, Mn atoms in each Mn row (normal to the plane of the paper in Figure 1) have the same spin direction but have opposite spin direction with respect to its nearest-neighbor Mn row. In addition, total energies of the cluster as a function of given magnetic moments are obtained, and the corresponding (random) spin arrangements obtained from the DFT optimization with fixed total magnetic moment (but without enforcing any constraint on spin direction on each Mn atom) are named as pattern C (Figure 1). It can be seen that the spin configurations corresponding to the pattern A typically possess lower energies than patterns B and C, and those corresponding to the pattern B have higher energies. After extensive DFT calculations for numerous spin arrangements in patterns A−C, we find that configuration A1 possesses the lowest energy (Figure 1), where every Mn atom entails opposite spin direction with respect to its nearest-neighbor Mn atoms. As a result, 34 Mn atoms are in spin-up and 33 atoms are in spin-down state so that the total magnetic moment of the cluster is quite small (6.9 $\mu_B$). Besides this AFM configuration, two mixed AFM-FM configurations (A2 and A3 in Figure 1) also have lower energies than other spin configurations (A2 and A3 are about only 6 meV/atom higher than A1). Here, configurations A2 and A3 are obtained by randomly flipping spin of a number of Mn atoms from spin-up to spin-down direction. The magnetic moment per Mn atom for A2 and A3 is 0.487 and 2.267 $\mu_B$, respectively. For the pattern B, the lowest-energy configuration is B1, which is 20.7 meV/atom higher in energy than A1. Note that B1 and a number of other configurations belonging to the B pattern are obtained by randomly flipping spin of one row of Mn atoms from spin-up to spin-down direction. There are four additional spin configurations belonging to pattern B, which have nearly degenerate energies. The energies of all these five configurations

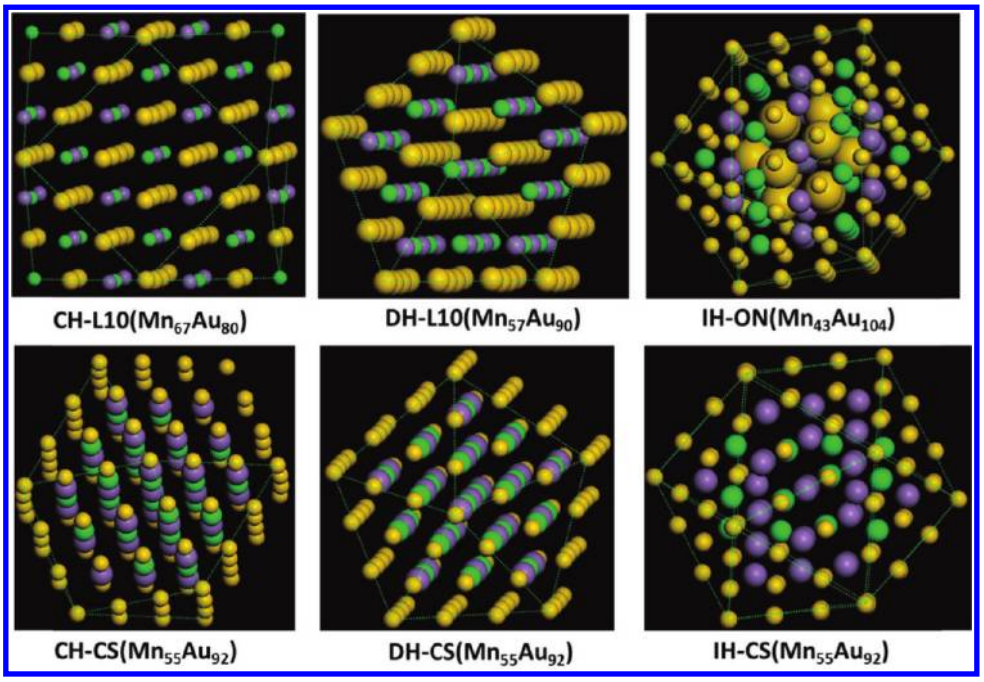


**Figure 2. Predicted lowest-energy spin configurations for 147 atom clusters in six highly symmetric morphologies. Yellow spheres (small and big) represent gold atoms, and purple and green spheres represent Mn atoms in spin-up and spin-down state, respectively. The big yellow spheres shown in IH-ON morphology highlight the inner gold shell in onion-like morphology.**

are also very close to that of the perfect FM configuration C2 (see Figure 1). As for pattern C, there are a number of spin configurations that are nearly degenerate in energy. Typically, their energies are about 11 meV/atom higher than that of A1. Ferromagnetic state (C2) can be obtained only when the total magnetic moment is fixed at a value >200 $\mu_B$, following the first approach elucidated in the Methods section.

For five other highly symmetric morphologies of the 147 atom clusters, extensive searches have also been carried out to attain the lowest-energy spin arrangements (see Supporting Information). Note that to enforce the symmetrical distribution of Mn atoms, the Mn/Au ratios of these clusters are mostly different (except for the three core–shell clusters). The lowest-energy spin configurations for the six morphologies are shown in Figure 2, where one can see that, for all the morphologies considered, AFM spin arrangements are the most preferred. Because of the differences in Mn/Au ratio or in Mn distribution for the six morphologies, the average magnetic moment per Mn atom is different as well, which is 0.023, 0.176, 0.180, 0.599, and 1.125 $\mu_B$ for the lowest-energy spin configuration of DH-$L1_0$, DH-CS, IH-ON, CH-CS, and IH-CS clusters, respectively. In particular, because DH-$L1_0$ and DH-CS clusters have identical decahedron structure and nearly the same Mn/Au ratio, the conclusion that the average magnetic moment per Mn atom for the core–shell morphology is much larger than the $L1_0$ morphology is consistent with previous one that the core–shell morphology can entail relatively higher (if not the highest) total magnetic moment.[7] We point out here that we have also examined paramagnetic states of 147 atom MnAu nanoclusters. We find that total energies of the paramagnetic states are much higher than those of the FM and AFM states. Hereafter, we will not discuss the paramagnetic states for other-sized MnAu nanoclusters.

**Relative Stabilities of 2.3–2.9 nm Nanoclusters with Six Different Morphologies.** We have also performed first-principles-based structural optimization of larger MnAu nanoclusters with 309 atoms (~2.3 nm) and 561 atoms (~2.9 nm) in six different morphologies to achieve an initial understanding of size- and shape-dependent relative stabilities. To this end, we employ the same lowest-energy spin arrangement for clusters with identical highly symmetric morphologies as the 147 atom nanoclusters (Figures 3 and 4). The calculated binding energies per atom for these clusters are shown in Figure 5. In view of the trend of binding energy change as a function of size, clearly the binding energies of the core–shell clusters decrease monotonically as their sizes increase from 55 atoms (~1.0 nm) to 561 atoms (~2.9 nm), whereas those of the CH-$L1_0$, DH-$L1_0$, and IH-ON clusters increase monotonously. These results suggest that the core–shell morphology becomes increasingly less favorable as the size increases toward 2–3 nm or as the Mn/Au ratio becomes greater than 1. Note that the core–shell morphology illustrated in Figures 3 and 4 represents perfect surface segregation of gold component. Previously, we have shown that highly symmetric

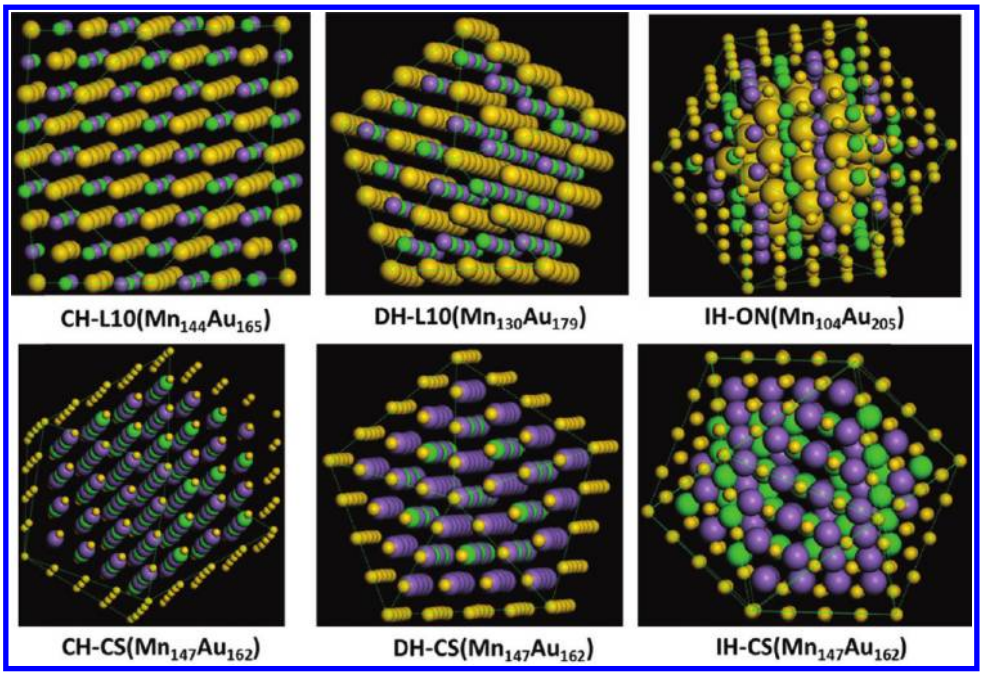


**Figure 3. Predicted lowest-energy spin configurations for 309 atom clusters in six highly symmetric morphologies.**

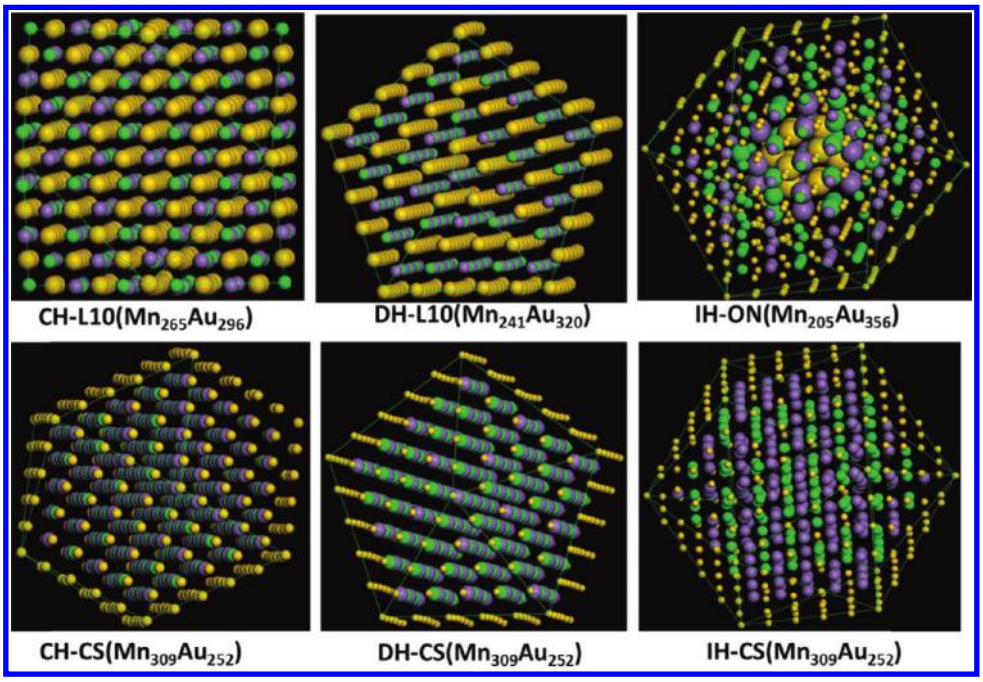


**Figure 4. Predicted lowest-energy spin configurations for 561 atom clusters in six highly symmetric morphologies.**

surface segregation morphology is energetically favorable when the size of the cluster is less than 1 nm.[7]

From Figure 5, one can also find that clusters with the $L1_0$ structure become increasingly favorable as the size increases and as the Mn/Au ratio is closer to 1:1. As the size increases from 55 atoms (~1.0 nm) to 147 atoms (~1.7 nm), it seems that both the highly symmetric $L1_0$ and core–shell morphologies are competitive with each other, and as the size increases to 309 atoms (~2.3 nm), the highly symmetric $L1_0$ morphology becomes more preferred than the highly symmetric core–shell morphology. These results suggest that, when synthesizing MnAu clusters in the size range of 2–3 nm and with Mn/Au ratio close to 1:1, clusters with $L1_0$ morphology are expected to be prevalent (see below). On the other hand, if the size of clusters is less than 1 nm and the Mn/Au ratio is less than 1:3, the core–shell clusters are expected to be dominant in the population.

**Relative Stabilities of 1.0–2.3 nm Nanoclusters with the Same Mn/Au Ratio.** Note that among the highly

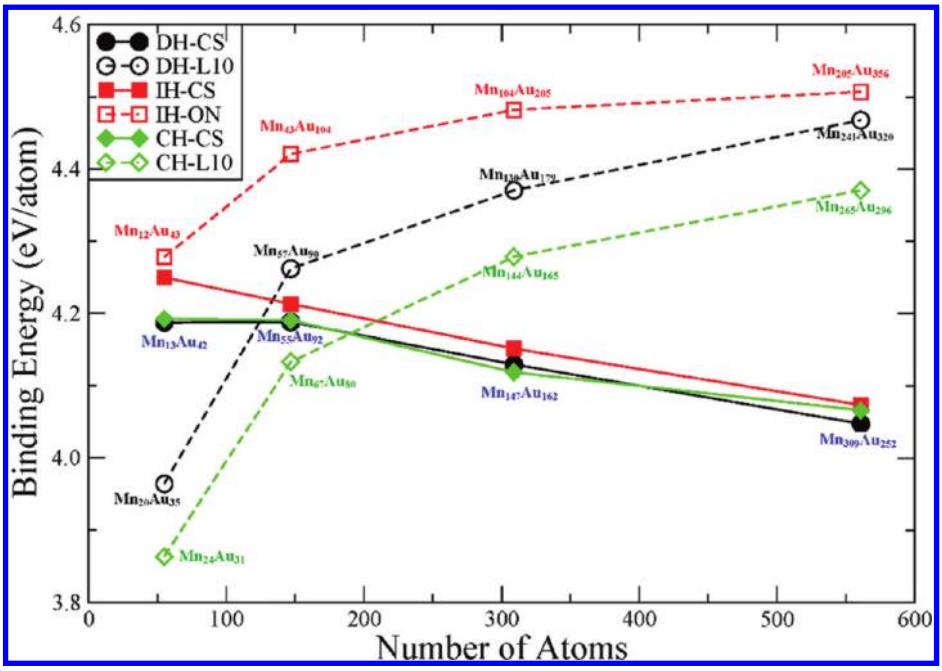


**Figure 5. Calculated binding energies of MnAu magic-number (55, 147, 309, and 561) clusters with six highly symmetric morphologies.**

**TABLE 1. Calculated Binding (or Cohesive) Energies (eV/atom) of Magic-Number Clusters with Different Morphologies but the Same Mn/Au Ratio in Each Subgroup[a]**

| | group I | | | group II | | | group III | | |
|---|---|---|---|---|---|---|---|---|---|
| | $E_b$ (eV/atom) | | | $E_b$ (eV/atom) | | | $E_b$ (eV/atom) | | |
| *N* | 55 | 147 | 309 | 55 | 147 | 309 | 55 | 147 | 309 |
| $d_{max}$ (nm) | ~1.0 | ~1.7 | ~2.3 | ~1.0 | ~1.7 | ~2.3 | ~1.0 | ~1.7 | ~2.3 |
| Mn/Au | 24:31 | 67:80 | 144:165 | 13:42 | 55:92 | 147:162 | 12:43 | 43:104 | 104:205 |
| CH-CS | 3.812 | 4.044 | 4.149 | 4.192 | 4.194 | 4.118 | 4.220 | 4.320 | 4.409 |
| CH-$L1_0$ | **3.863** | **4.133** | **4.278** | 4.203 | 4.290 | **4.252** | 4.231 | 4.426 | 4.513 |
| DH-CS | 3.798 | 4.037 | 4.128 | 4.187 | 4.190 | 4.129 | 4.212 | 4.353 | 4.376 |
| DH-$L1_0$ | 3.818 | **4.133** | 4.221 | 4.211 | **4.308** | 4.213 | 4.236 | **4.440** | **4.529** |
| IH-CS | **3.864** | 4.078 | 4.170 | **4.250** | 4.222 | 4.151 | **4.280** | 4.377 | 4.424 |
| IH-ON | 3.843 | 4.104 | 4.223 | **4.246** | 4.271 | 4.201 | **4.278** | 4.421 | 4.482 |

[a] Nine Mn/Au ratios are considered. Group I, clusters with identical Mn/Au ratio as the highly symmetric CH-$L1_0$ morphology; group II, clusters with identical Mn/Au ratio as the highly symmetric IH-CS morphology; and group III, clusters with identical Mn/Au ratio as the highly symmetric IH-ON morphology. Clusters with the greatest binding energies (including nearly degenerate ones whose $E_b$ difference is <5 meV/atom) are highlighted in bold; $d_{max}$ refers to the maximum distance between two atoms in every nanocluster.

symmetric clusters shown in Figures 2–4, the binding (or cohesive) energies of the IH-ON clusters seem always the greatest regardless of their sizes (Figure 5). This is largely due to the relatively small Mn/Au ratios required to construct the IH-ON clusters with highly symmetric morphology. To attain a more reasonable assessment of relative stabilities among clusters with the same size but different morphologies, we have constructed various nanoclusters with the same Mn/Au ratio but less symmetric morphologies (*i.e.*, Mn distribution is less symmetric). To this end, some Au atoms in the surface layers are converted to Mn atoms or *vice versa*, while the core part still retains highly symmetric morphologies. We organize 55, 147, and 309 atom clusters with nine different Mn/Au ratios into three groups: (I) clusters with identical Mn/Au ratio as the highly symmetric CH-$L1_0$ morphology, that is, $Mn_{24}Au_{31}$, $Mn_{67}Au_{80}$, and $Mn_{144}Au_{165}$; (II) clusters with identical Mn/Au ratio as the highly symmetric IH-CS morphology, that is, $Mn_{13}Au_{42}$, $Mn_{55}Au_{92}$, and $Mn_{147}Au_{162}$; and (III) clusters with identical Mn/Au ratio as the highly symmetric IH-ON morphology, that is, $Mn_{12}Au_{43}$, $Mn_{43}Au_{104}$, and $Mn_{104}Au_{205}$ (see Figure 5). Thus, from group I to III, the Mn composition for clusters with the same size decreases except $Mn_{147}Au_{162}$. Again, in these newly constructed clusters, the AFM spin configurations arefixed. Calculated binding energies of all clusters are presented in Table 1.

As shown in Table 1, for 55 atom clusters in group I, both CH-$L1_0$ and IH-CS clusters have the greatest binding energies; therefore, both $L1_0$ and core–shell morphologies are energetically preferred. As the cluster

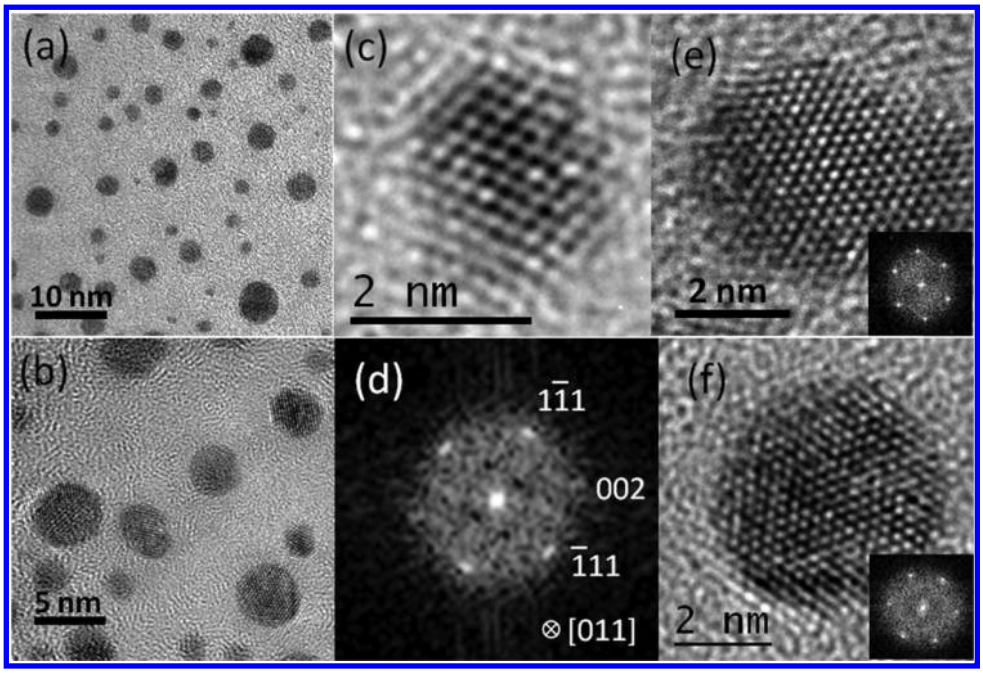


**Figure 6. (a,b) Transmission electron microscopy (TEM) images of as-prepared MnAu nanoparticles on amorphous carbon support film. High-resolution TEM images of (c) 1.8 nm, (e) 3.4 nm, and (f) 4.6 nm MnAu nanoparticles. (d) Fast Fourier transform (FFT) of image (c) showing the crystal lattice index. FFT of images (e) and (f) are shown in corresponding inset at the low-right corner.**

size increases to 147 atoms, both CH-$L1_0$ and DH-$L1_0$ clusters exhibit greatest binding energies, indicating that the $L1_0$ morphology indeed becomes increasingly favorable, whereas the core–shell and icosahedron onion-like morphologies are less favored. When the size increases to 309 atoms, the CH-$L1_0$ cluster still possesses the greatest binding energy. Thus, the cuboctahedron $L1_0$ morphology appears always favorable from 1.7 to 2.3 nm size range, at least when the Mn/Au ratio is close to 1:1 (the Mn/Au ratio for the 147 and 309 atom structures in group I is 0.84 and 0.87, respectively).

For 55 atom clusters in group II, the IH-CS and IH-ON clusters have the greatest binding energy (Table 1). Again, this result is consistent with the previous study[7] in that highly symmetric core–shell morphology is energetically favorable when the size of cluster is less than 1 nm. Note that the 55 atom onion-like cluster is essentially like the 55 atom core–shell cluster except that the center atom is Au, while two Au atoms on the outer shell are converted to Mn atoms. As the size increases to 147 atoms, the core–shell morphology yields to the $L1_0$ morphology in stability as the DH-$L1_0$ cluster possesses the greatest binding energy (Table 1). When the size increases to 309 atoms and the Mn/Au ratio (147:162) is closer to 1, as expected, the CH-$L1_0$ cluster becomes the most preferred. In any case, for group II clusters, the onion-like morphology is less preferred than others when the size is greater than 1.7 nm.

For 55 atom clusters in group III, because the core–shell and onion-like morphologies are nearly the same, both IH-CS and IH-ON clusters are expected to be the most favorable. As the size increases to 147 atoms, notably, the DH-$L1_0$ cluster has a larger binding energy than the IH-ON cluster, even the Mn/Au ratio used in this case is based on that of the IH-ON cluster. Hence, the onion-like morphology appears to be less favorable than the $L1_0$ morphologies when the cluster size is greater than 1.7 nm, regardless of the Mn/Au ratio. When the size increases to 309 atoms, the DH-$L1_0$ cluster still has the greatest binding energy. So, for clusters in the size range of 1.7–2.3 nm and with Mn/Au ratio close to 1:2, decahedron $L1_0$ morphology should be dominant in the cluster population.

In summary, by examining relative stabilities of clusters with different morphologies but the same Mn/Au ratio in the same subgroup, we find that with small sizes (<1 nm), the icosahedron core–shell morphology is the most preferred, while in the size range of 1.7–2.3 nm, the $L1_0$ morphologies are the most preferred. In particular, if the Mn/Au ratio is close to 1:1, the cuboctahedron $L1_0$ morphology is more favorable than others, while if the Mn/Au ratio is close to 1:2, decahedron $L1_0$ morphology becomes the most favorable. Our conclusions are consistent with the experimental characterization of MnAu nanoparticles of sizes 1.8–4.6 nm (see below).

**Experimental Characterization of MnAu Nanoparticles with Sizes of 1–5 nm.** Recently, we reported an experimental study of MnAu nanoparticles with average sizes ranging from 5 to 10 nm.[25] In that experiment, we observed a major structural change in the nanoparticles, that is, from the bulk-like $\beta_2$ structure in 10 nm particles to $L1_0$ structure[25] in 5 nm particles. For the first-principles

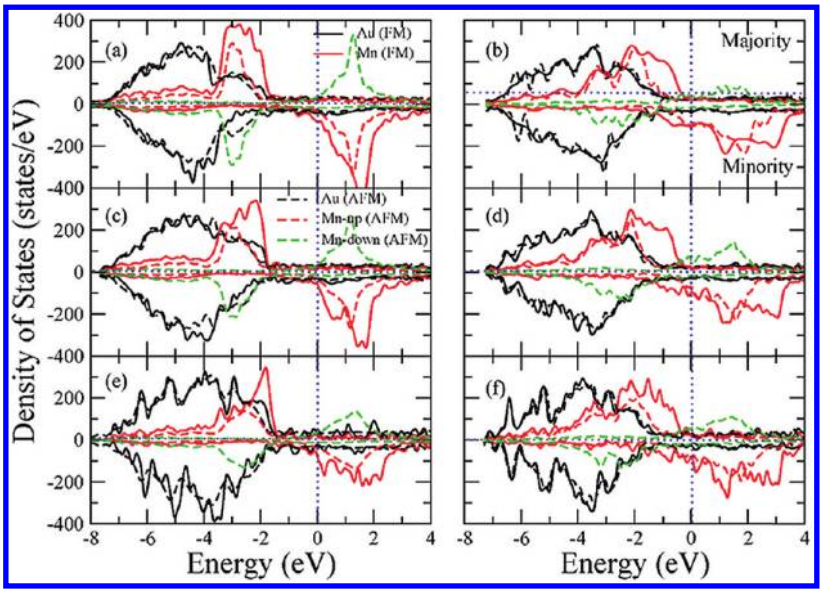


**Figure 7. Projected density of states of 309 atom clusters shown in Figure 3: (a) CH-$L1_0$; (b) CH-CS; (c) DH-$L1_0$; (d) DH-CS; (e) IH-ON; (f) IH-CS.**

study, however, the size of nanoclusters has to be limited to be less than 3 nm due to high computing costs. To confirm the predicted structural properties of nanoclusters presented above, we have carefully chosen a few relatively small nanoparticles in the size range of 1.8−4.6 nm from the same cluster samples produced in the previous study for further high-resolution transmission electron microscopy (HR-TEM) characterization. Figure 6a,b shows the TEM image of the nanoparticles with size varying approximately from 1 to ∼5 nm. Typical nanoparticles with sizes of 1.8, 3.4, and 4.6 nm were also observed using HR-TEM, as shown in Figure 6c,e,f, respectively. The crystal lattices were clearly resolved in these high-resolution images, indicating that the nanoparticles were single crystals and showing nearly identical structures. By indexing the fast Fourier transform (FFT) of Figure 6c, as shown in Figure 6d, and measuring the corresponding lattice spacings, the nanoparticle can be determined to be a slightly tetragonalized fcc structure with lattice constants $a$ = 0.418 nm and $c$ = 0.388 nm. Similar analysis was performed on the other two HR-TEM images, which confirmed the identical structure, but with slightly different lattice constants: $a$ = 0.403 nm and $c$ = 0.396 nm for the 3.4 nm nanoparticle, and $a$ = 0.395 nm and $c$ = 0.438 nm for the 4.6 nm nanoparticle.

The tetragonal fcc structure and lattice constants experimentally determined here for the 1.8 nm MnAu nanoparticle is virtually identical to a cuboctahedral $L1_0$ morphology predicted above for the 147 atom nanocluster (∼1.7 nm) whose calculated lattice constants are $a \sim 0.413$ nm, $c \sim 0.377$ nm, suggesting the 1.8 nm MnAu nanocluster exhibits cuboctahedral $L1_0$ morphology. Note that our first-principles calculation suggests that, if the Mn/Au ratio is close to 1:1, the cuboctahedron $L1_0$ morphology is the most favorable for MnAu nanoclusters beyond the size 1.7 nm. We have measured the lattice constants of a fully optimized CH-$L1_0$ $Mn_{144}Au_{165}$ cluster (the optimization was accomplished with a tight convergence criterion), that is, $a \sim 0.412$ nm and $c \sim 0.382$ nm. These values are close to the experimentally measured values for the 3.4 nm nanoparticle.

Note also that an energy-dispersive X-ray spectroscopy (EDS) analysis indicates that the relatively larger experimental nanoparticles (>5 nm) are slightly Mn-rich (Mn/Au ratio ∼1.3). Nevertheless, the $L1_0$ structure is stable in other systems over a range of compositions near the 1:1 stoichiometry, so it is not unreasonable that it is stable here at off-stoichiometric compositions. For example, in the FePt system, the $L1_0$ forms at compositions from ∼37 to ∼57 atom % Pt.[26] Furthermore, we have examined relative stabilities of a number of less symmetric 309 atoms morphologies with the Mn/Au ratio of 57:43. The initial structures are constructed by converting some Au atoms in the surface of highly symmetric morphologies into Mn atoms at random. Calculated binding energies per atom for the 309 atom CH-$L1_0$, CH-CS, DH-$L1_0$, DH-CS, IH-ON, and IH-CS structures are 3.989, 3,953, 3.989, 3.924, 3.980, and 3.970 eV/atom, respectively. Hence, in modest Mn-rich conditions, the $L1_0$ morphologies still appear to be the most preferred, at least for the 2.3 nm MnAu nanoclusters, consistent with experimental observations.

**Electronic and Magnetic Properties.** Using 309 atom clusters with highly symmetric morphologies (Figure 3) as representative clusters, their element-projected electronic density of states (DOS) are plotted in Figure 7. For the clusters being in the AFM state, the projected

**TABLE 2. Calculated Magnetic Moments per Mn Atom for Magic-Number Clusters in Six Highly Symmetric Morphologies (Figures 2–4) and in Ferromagnetic and Antiferromagnetic State, Respectively ($d_{max}$ Refers to the Maximum Distance between Two Atoms in Every Nanocluster)**

| | magnetic moment ($\mu_B$/Mn) | | | | magnetic moment ($\mu_B$/Mn) | | | |
|---|---|---|---|---|---|---|---|---|
| | ferromagnetic | | | | antiferromagnetic | | | |
| $N$ | 55 | 147 | 309 | 561 | 55 | 147 | 309 | 561 |
| $d_{max}$ (nm) | ~1.0 | ~1.7 | ~2.3 | ~2.9 | ~1.0 | ~1.7 | ~2.3 | ~2.9 |
| CH-CS | 4.224 | 3.837 | 3.791 | 3.718 | 1.434 | 1.107 | 1.738 | 0.327 |
| CH-$L1_0$ | 4.609 | 4.424 | 4.340 | 4.304 | 0.0 | 0.103 | 0.0 | 0.058 |
| DH-CS | 3.923 | 3.823 | 3.844 | 3.789 | 0.730 | 1.375 | 1.059 | 0.018 |
| DH-$L1_0$ | 4.349 | 4.420 | 4.305 | 4.296 | 0.0 | 0.766 | 0.0 | 0.026 |
| IH-CS | 4.23 | 3.735 | 3.797 | 3.789 | 0.002 | 0.955 | 0.930 | 0.653 |
| IH-ON | 4.25 | 4.142 | 4.189 | 4.145 | 0.0 | 0.110 | 0.066 | 0.094 |

**TABLE 3. Calculated Binding Energy Difference between the Antiferromagnetic and Ferromagnetic States, $\Delta E_b = \Delta E_{bAFM} - \Delta E_{bFM} = (E_{FM} - E_{AFM})/N$, the Energy Difference per Mn Atom, $\Delta E_{pMn} = (E_{FM} - E_{AFM})/N_{Mn}$, and the Estimated Curie ($T_c$) or Neél ($T_N$) Temperature (K) ($d_{max}$ Refers to the Maximum Distance between Two Atoms in Every Nanocluster)**

| | $d_{max}$ (nm) | $N$ | $\Delta E_b$ (meV) | $\Delta E_{pMn}$ (meV) | $T_c$ or $T_N$ (K) | | $N$ | $d_{max}$ (nm) | $\Delta E_b$ (meV) | $\Delta E_{pMn}$ (meV) | $T_c$ or $T_N$ (K) |
|---|---|---|---|---|---|---|---|---|---|---|---|
| CH-CS | ~1.0 | 55 | 10.9 | 46.0 | 356 | CH-$L1_0$ | 55 | ~1.0 | 17.4 | 38.4 | 297 |
| | ~1.7 | 147 | 27.3 | 73.0 | 564 | | 147 | ~1.7 | 22.4 | 49.2 | 380 |
| | ~2.3 | 309 | 35.8 | 75.3 | 582 | | 309 | ~2.3 | 26.8 | 57.4 | 444 |
| | ~2.9 | 561 | 68.1 | 123.7 | 956 | | 561 | ~2.9 | 29.1 | 61.7 | 477 |
| DH-CS | ~1.0 | 55 | 17.1 | 72.3 | 559 | DH-$L1_0$ | 55 | ~1.0 | 2.8 | 7.8 | 60 |
| | ~1.7 | 147 | 28.3 | 75.5 | 583 | | 147 | ~1.7 | 9.3 | 23.9 | 185 |
| | ~2.3 | 309 | 52.0 | 109.4 | 846 | | 309 | ~2.3 | 29.6 | 70.3 | 543 |
| | ~2.9 | 561 | 55.8 | 101.4 | 784 | | 561 | ~2.9 | 34.9 | 81.4 | 629 |
| IH-CS | ~1.0 | 55 | 18.8 | 79.7 | 616 | IH-ON | 55 | ~1.0 | 24.7 | 113 | 873 |
| | ~1.7 | 147 | 18.6 | 49.7 | 384 | | 147 | ~1.7 | **28.7** | 98.0 | 757 |
| | ~2.3 | 309 | 54.7 | 115.0 | 889 | | 309 | ~2.3 | **23.0** | 68.3 | 527 |
| | ~2.9 | 561 | 71.0 | 130.6 | 1009 | | 561 | ~2.9 | **12.8** | 35.0 | 270 |

DOS contributed by Mn atoms with up-spin and down-spin are also plotted separately. Clearly, the projected DOS by Au atoms in FM and AFM configurations is very similar. Thus, Au atoms have little influence on the relative stability between the FM and AFM states. For Mn atoms, in contrast, some higher-energy majority spin states of Mn atoms in the FM configurations turn into lower-energy minority states in the AFM configuration, resulting in lowered total energy with AFM configurations.

The magnetic moments per Mn atom for the clusters in FM and AFM states are both listed in Table 2. In FM states, the magnetic moment decreases uniformly as the size increases for each morphological structure, and the magnetic moments of $L1_0$ and onion-like morphologies are notably larger than the corresponding core–shell morphologies. This is because alternating distribution of Au and Mn shells or slabs (superlattices) is helpful for the parallelization of spins between neighboring Mn atoms. Conversely, in AFM states, the average magnetic moments per Mn atom are almost zero for both $L1_0$ and onion-like morphologies. No obvious trend in magnetic moments is found as the size increases. The differences in magnetic moments between the FM and AFM states are also reflected in the DOS. In Figure 7, it is clear that for CH-$L1_0$, DH-$L1_0$, and IH-ON clusters the majority states of the spin-up Mn atoms and the minority states of the spin-down Mn are almost the same near the Fermi level. This is why the net magnetic moments of the $L1_0$ and onion-like morphologies are nearly zero. On the other hand, for the core–shell morphologies, the minority states of spin-down Mn atoms blow the Fermi level are usually much less than the majority states of spin-up Mn atoms. A reason may be that the number of spin-up and spin-down Mn atoms are different, or values of local magnetic moments on Mn atoms within different shells are different.

The higher stability of CH-$L1_0$ and DH-$L1_0$ MnAu nanoclusters compared to other morphologies renders them potential candidates for magnetic nanoparticle applications if their FM states can be stabilized. However, FM states are only metastable compared to the AFM states for the size of clusters considered (1.0–2.9 nm). In Table 3, we list calculated binding energy difference ($\Delta E_b$) between the FM and AFM

states. Apparently, except for IH-ON, $\Delta E_b$ of all clusters increases almost monotonously with increasing the size. Moreover, $\Delta E_b$ values of $L1_0$ and onion-like morphologies are all less than that of the core–shell morphologies for $N \geq 309$. Because the binding energy differences between AFM and FM states for the ordered $L1_0$ clusters in the size range of 2.3–2.9 nm are on the order of 300–400 K in temperature units, the FM states may be realized at the room temperature.

Another general feature for magnetic materials is that they undergo a transformation into the paramagnetic state when the temperature is above the Curie or Neél temperatures. Materials with higher Curie or Neél temperatures are important for applications. Values of Curie or Neél temperatures are related to the exchange interactions between adjacent magnetic atoms. In MnAu nanoclusters, only Mn atoms possess magnetic moments in either FM or AFM states. The energy difference per Mn atom ($\Delta E_{pMn}$) between the FM and AFM state can be used to estimate effective exchange interaction between adjacent Mn atoms, thereby the Curie or Neél temperatures of MnAu nanoclusters. Calculated $\Delta E_{pMn}$ are given in Table 3. It can be seen that $\Delta E_{pMn}$ values of the core–shell clusters are usually greater than other clusters. $\Delta E_{pMn}$ increases uniformly with increasing the size except IH-ON. Using the formula $3/2k_BT_{C(N)} = \Delta E_{pMn}$, calculated Curie (Neél) temperatures[27,28] are also listed in Table 3. For $L1_0$ clusters with size $N \geq 309$, the estimated Curie or Neél temperatures are higher than 400 K, suggesting that the FM or AFM states of larger-sized $L1_0$ MnAu nanoclusters are thermally stable at the room temperature. Overall, our calculations suggest that $L1_0$ nanoclusters in the size range of 2.3–2.9 nm are most favorable.

## CONCLUSIONS

We have investigated low-lying spin configurations in MnAu magic-number nanoclusters with highly symmetric morphologies. We find that the lowest-energy spin configurations are all antiferromagnetic. On the basis of the lowest-energy spin configurations, energy ranking among MnAu nanoclusters with the same Mn/Au ratio and size but different morphologies is also determined. When the size of cluster is less than 1 nm, the core–shell morphology is more favorable, whereas when the size of cluster is in the range of 1.7–2.9 nm, the $L1_0$ morphologies become more favorable. More specifically, the decahedron $L1_0$ morphology is energetically more preferred when the Mn/Au ratio is close to 1:2, whereas the cuboctahedron $L1_0$ morphology is more preferred when the Mn/Au ratio is close to 1:1. Our conclusions appear to be consistent with the experimental characterization of MnAu nanoparticles of sizes 1.8–4.6 nm. The $L1_0$ morphologies may possess very high magnetic moments if stabilized in the metastable ferromagnetic states. The AFM or FM magnetic state is likely to be stable at room temperature according to the estimated Curie and Neél temperature. Because their closeness in binding energies, there is possible existence of both AFM and FM states for $L1_0$ MnAu nanoclusters in different sizes, and this mixed system could be useful for certain applications such as exchange bias.[29–31]

## METHODS

DFT calculations were carried out using a linear combination of atomic orbital method implemented in SIESTA package,[32] within the spin-polarized generalized gradient approximation (GGA) of Perdew–Burke–Ernzerhof (PBE).[33] Norm-conserving scalar relativistic pseudopotentials generated from the atomic valence configurations $5d^{10}6s^1$ and $3d^54s^2$ for Au and Mn, respectively, by the Troullier–Martins scheme[34,35] were employed, for which core corrections were included. Split valence double-$\zeta$ basis sets plus polarization (DZP) were selected for the DFT calculation. A real space grid with an equivalent cutoff of 250 Ry was adopted to expand the electron density for numerical integration. This cutoff has been tested to ensure that no significant changes in total energy with increasing the value of cutoff. The supercell adopted for each MnAu nanocluster is sufficiently large to ensure the interaction between the nanocluster, and its image in the neighbor cells is negligible. Only the $\Gamma$ point was adopted for k-point sampling during both the structural optimization and electronic structure calculations. Moreover, to ensure that the predicted magnetic properties based on the SIESTA package are reliable, we also perform cross-checking calculations using the VASP package (see Supporting Information). The predicted energy rankings and magnetic moments of different structures are consistent with those based on SIESTA calculations.

Experimentally, MnAu nanoparticles were deposited from a Mn/50 atom % Au alloy target, *via* inert gas condensation in a cluster deposition system with a base pressure of $10^{-8}$ Torr.[36] We used an RF sputtering gun, positioned perpendicular to the cluster source, to alternately deposit C or $SiO_2$ thin films in order to provide a thin protective layer to prevent oxidation. The structure and morphology of the nanoparticles were characterized by TEM and HR-TEM, accomplished with a JEOL 2010 FEG TEM (at Arizona State University) operated at 200 kV. The nanoparticles were directly deposited onto amorphous carbon support films.

*Acknowledgment.* This work was supported by grants from the NSF (DMR-0820521 and EPS-1010674) and ARL (W911NF1020099), and by the University of Nebraska's Holland Computing Center.

*Supporting Information Available:* Illustrations of various spin configurations examined for 147 atom clusters with highly symmetric morphologies and their relative energies, and a comparison between SIESTA and VASP calculation results are collected. This material is available free of charge *via* the Internet at http://pubs.acs.org.

## REFERENCES AND NOTES

1. Nayak, S. K.; Nooijen, M.; Jena, P. Isomerism and Novel Magnetic Order in $Mn_{13}$ Cluster. *J. Phys. Chem. A* **1999**, *103*, 9853–9856.
2. Bobadova-Parvanova, P.; Jackson, K. A.; Srinivas, S.; Horoi, M. Emergence of Antiferromagnetic Ordering in Mn Clusters. *Phys. Rev. A* **2003**, *67*, 061202(R).
3. Bobadova-Parvanova, P.; Jackson, K. A.; Srinivas, S.; Horoi, M. Structure, Bonding, and Magnetism in Manganese Clusters. *J. Chem. Phys.* **2005**, *122*, 014310.
4. Knickelbein, M. B. Experimental Observation of Superparamagnetism in Manganese Clusters. *Phys. Rev. Lett.* **2001**, *86*, 5255–5257.

5. Knickelbein, M. B. Magnetic Ordering in Manganese Clusters. *Phys. Rev. B* **2004**, *70*, 014424.
6. Datta, S.; Kabir, M; Mookerjee, A.; Saha-Dasgupta, T. Engineering the Magnetic Properties of the $Mn_{13}$ Cluster by Doping. *Phys. Rev. B* **2011**, *83*, 075425.
7. Wang, J; Bai, J.; Jellinek, J.; Zeng, X. C. Gold-Coated Transition-Metal Anion $[Mn_{13}@Au_{20}]^-$ with Ultrahigh Magnetic Moment. *J. Am. Chem. Soc.* **2008**, *129*, 4110–4111.
8. Ferrando, R.; Jellinek, J; Johnston, R. L. Nanoalloys: From Theory to Applications of Alloy Clusters and Nanoparticles. *Chem. Rev.* **2008**, *108*, 846–910.
9. Rossi, G.; Rapallo, A.; Mottet, C.; Fortunelli, A.; Baletto, F.; Ferrando, R. Magic Polyicosahedral Core−Shell Clusters. *Phys. Rev. Lett.* **2004**, *93*, 105503.
10. Ferrando, R.; Fortunelli, A.; Rossi, G. Quantum Effects on the Structure of Pure and Binary Metallic Nanoclusters. *Phys. Rev. B* **2005**, *72*, 085449.
11. Fernández, E. M.; Balbás, L. C.; Pérez, L. A.; Michaelian, K.; Garzón, I. L. Structural Properties of Bimetallic Clusters from Density Functional Calculations. *Int. J. Mod. Phys. B* **2005**, *19*, 2339–2344.
12. Jiang, Z.-Y.; Lee, K.-H.; Li, S.-T.; Chu, S.-Y. Structures and Charge Distributions of Cationic and Neutral $Cu_{n-1}Ag$ clusters ($n$=2−8). *Phys. Rev. B* **2006**, *73*, 235423.
13. Rapallo, A.; Rossi, G.; Ferrando, R.; Fortunelli, A.; Curley, B. C.; Lloyd, L. D.; Tarbuck, G. M.; Johston, R. L. Global Optimization of Bimetallic Cluster Structures. I. Size-Mismatched Ag−Cu, Ag−Ni, and Au−Cu Systems. *J. Chem. Phys.* **2005**, *122*, 194308.
14. Darby, S.; Mortimer-Jones, T. V.; Johnston, R. L.; Roberts, C. Theoretical Study of Cu−Au Nanoalloy Clusters Using a Genetic Algorithm. *J. Chem. Phys.* **2002**, *116*, 1536.
15. Lordeiro, R. A.; Guimarães, F. F.; Belchior, J. C.; Johnston, R. L. Determination of Main Structural Compositions of Nanoalloy Clusters of $Cu_xAu_y$ ($x + y \leq 30$) Using a Genetic Algorithm Approach. *Int. J. Quantum Chem.* **2003**, *95*, 112–125.
16. Wang, G.-F.; Van Hove, M. A.; Ross, P. N.; Baskes, M. I. Monte Carlo Simulations of Segregation in Pt−Ni Catalyst Nanoparticles. *J. Chem. Phys.* **2005**, *122*, 024706.
17. Mottet, C.; Tréglia, G.; Legrand, B. Theoretical Investigation of Chemical and Morphological Ordering in $Pd_cCu_{1-c}$ Clusters. *Phys. Rev. B* **2002**, *66*, 045413.
18. Rubinovich, L.; Haftel, M. I.; Bernstein, N.; Polak, M. Compositional Structures and Thermodynamic Properties of Pd−Cu, Rh−Pd, and Rh−Pd−Cu Nanoclusters Computed by a Combined Free-Energy Concentration Expansion Method and Tight-Binding Approach. *Phys. Rev. B* **2006**, *74*, 035405.
19. Liu, H. B.; Pal, U.; Medin, A.; Maldonado, C.; Ascencio, J. A. Structural Incoherency and Structure Reversal in Bimetallic Au−Pd Nanoclusters. *Phys. Rev. B* **2005**, *71*, 075403.
20. Müller, M.; Albe, K. Lattice Monte Carlo Simulations of FePt Nanoparticles: Influence of Size, Composition, and Surface Segregation on Order−Disorder Phenomena. *Phys. Rev. B* **2005**, *72*, 094203.
21. Alloyeau, D.; Ricolleau, C.; Mottet, C.; Oikawa, T.; Langlois, C.; Bouar, Y. L.; Braidy, N.; Loiseau, A. Size and Shape Effects on the Order−Disorder Phase Transition in CoPt Nanoparticles. *Nat. Mater.* **2009**, *8*, 940–946.
22. Bochicchio, D.; Ferrando, R. Size-Dependent Transition to High-Symmetry Chiral Structures in AgCu, AgCo, AgNi, and AuNi Nanoalloys. *Nano Lett.* **2010**, *10*, 4211–4216.
23. Gruner, M. E.; Rollmann, G.; Entel, P.; Farle, M. Multiply Twinned Morphologies of FePt and CoPt Nanoparticles. *Phys. Rev. Lett.* **2008**, *100*, 087203.
24. Rossi, G.; Ferrando, R; Mottet, C. Structure and Chemical Ordering in CoPt Nanoalloys. *Faraday Discuss.* **2008**, *138*, 193–210.
25. Wei, X.; Le Roy, D.; Skomski, R.; Li, X. Z.; Sun, Z.; Shield, J. E.; Kramer, M. J.; Sellmyer, D. J. Structure and Magnetism of MnAu Nanoclusters. *J. Appl. Phys.* **2011**, *109*, 07B523.
26. Moffatt, W. G. *The Handbook of Binary Phase Diagrams*; Genium Publishing Corporation: New York, 1984; Vol. 3, 7/84.
27. Li, L.; Qin, R.; Li, H.; Yu, L.; Liu, Q.; Luo, G.; Gao, Z.; Lu, J. Functionalized Graphene for High-Performance Two-Dimensional Spintronics Devices. *ACS Nano* **2011**, *5*, 2601–2610.
28. Kudrnovsky, J.; Turek, I.; Drchal, V.; Maca, F.; Masek, J.; Weinberger, P.; Bruno, P. *Ab Initio* Study of Curie Temperatures of Diluted Magnetic Semiconductors. *J. Supercond.* **2003**, *16*, 119–122.
29. Park, B. G; Wunderlich, J.; Martí, X; Holý, V.; Kurosaki, Y.; Yamada, M.; Yamamoto, H.; Nishide, A.; Hayakawa, J.; Takahashi, H.; Shick, A. B.; Jungwirth, T. A Spin-Valve-like Magnetoresistance of an Antiferromagnet-Based Tunnel Junction. *Nat. Mater.* **2011**, *10*, 347–351.
30. Schmid, I.; Marioni, M. A.; Kappenberger, P.; Romer, S.; Parlinska-Wojtan, M.; Hug, H. J.; Hellwig, O.; Carey, M. J.; Fullerton, E. E. Exchange Bias and Domain Evolution at 10 nm Scales. *Phys. Rev. Lett.* **2010**, *105*, 197201.
31. Mishra, S. K.; Radu, F.; Dürr, H. A.; Eberhardt, W. Training-Induced Positive Exchange Bias in NiFe/IrMn Bilayers. *Phys. Rev. Lett.* **2009**, *102*, 177208.
32. Soler, J. M.; Artacho, J.; Gale, J. D.; García, A.; Junquera, J.; Ordejón, P.; Sánchez-Portal, D. J. The SIESTA Method for *Ab Initio* Order-N Materials Simulation. *J. Phys.: Condens. Matter* **2002**, *14*, 2745–2779.
33. Perdew, J. P.; Zunger, A. Self-Interaction Correction to Density-Functional Approximations for Many-Electron Systems. *Phys. Rev. B* **1981**, *23*, 5048–5079.
34. Troullier, N.; Martins, J. L. Efficient Pseudopotentials for Plane-Wave Calculations. *Phys. Rev. B* **1991**, *43*, 1993–2006.
35. Troullier, N.; Martins, J. L. Efficient Pseudopotentials for Plane-Wave Calculations. II. Operators for Fast Iterative Diagonalization. *Phys. Rev. B* **1991**, *43*, 8861–8869.
36. Xu, Y. F.; Yan, M. L.; Sellmyer, D. J. In *Advanced Magnetic Nanostuctures*; Sellmyer, D. J., Skomski, R., Eds.; Springer: Berlin, Germany, 2006; p 209.